ELSEVIER

Contents lists available at ScienceDirect

Materials Science & Engineering A

journal homepage: www.elsevier.com/locate/msea





Deformation mechanisms in crystalline-amorphous high-entropy composite multilayers

Li Jiang ^{a,b,*}, Zhitong Bai ^c, Max Powers ^b, Yue Fan ^c, Wei Zhang ^a, Easo P. George ^{d,e}, Amit Misra ^{b,c}

- ^a School of Materials Science and Engineering, Dalian University of Technology, Dalian, 116024, China
- b Department of Materials Science and Engineering, University of Michigan, Ann Arbor, MI, 48109, USA
- E Department of Mechanical Engineering, University of Michigan, Ann Arbor, MI, 48109, USA
- ^d Materials Science and Technology Division, Oak Ridge National Laboratory, Oak Ridge, TN, 37831, USA
- ^e Materials Science and Engineering Department, University of Tennessee, Knoxville, TN, 37996, USA

ARTICLE INFO

Keywords: High-entropy alloys Nanostructured metallic multilayers Crystalline-amorphous composite Deformation mechanism

ABSTRACT

Magnetron sputtering at room temperature was used to synthesize high-entropy composite multilayers (HECMs) with alternating layers of nominal composition CrMnFeCoNi and TiZrNbHfTa. HECMs with individual layer thickness of 50 nm exhibited an amorphous structure in the TiZrNbHfTa layers, and face-centered cubic (FCC) nanocrystalline structure with stacking faults and nanotwins in the CrMnFeCoNi layers. However, the HECMs with 5 nm individual layer thickness exhibited completely amorphous structures in both layers. Nanoindentation, followed by electron microscopy imaging of the indent plastic zone, was used to experimentally characterize the hardness and deformability. Molecular dynamics simulations were used to elucidate the deformation mechanisms. The high hardness of 7.8 GPa in the 5 nm layer thickness HECM is attributed to the amorphous structures in both layers with multiple shear bands around the indents. The 50 nm layer thickness HECM also exhibits high hardness of 5.6 GPa but with a more homogeneous spread of plasticity resulting in a reduced density of shear bands around indents. Strengthening in the 50 nm HECM results from a combined effect from the high density of stacking faults and nanotwins in CoCrFeMnNi, and the amorphous structure of the TiZrNbHfTa layers. The amorphous 50 nm TiZrNbHfTa nanolayers exhibit a heterogeneous nano-glass-type structure where the reorientation and agglomeration of amorphous zones seem to provide channels for plastic flow enabling enhanced deformability. Composite thin films of high entropy alloys exhibit a variety of fine structures, nanotwinned or homogeneous amorphous in CrMnFeCoNi, and heterogeneous amorphous in TiZrNbHfTa layers that enable new approaches to tune the strength and deformability.

1. Introduction

The concept of high-entropy alloys (HEAs) or multi-principal element alloys was first proposed by Cantor and Yeh et al. in 2004 [1, 2]. Since then, research on HEAs [3–6] has demonstrated superior properties such as excellent strength-ductility combination [7–10], thermal stability at high temperature [11,12] and good corrosion and wear resistance [13,14].

The extensively investigated Cantor alloy with the equiatomic composition CrMnFeCoNi can be cast, deformed and recrystallized into a single-phase face-centered cubic (FCC) crystal structure with superb mechanical properties, especially at 77 K, where the yield strength and

toughness are 750 MPa and 219 MPa m $^{1/2}$, respectively [6]. Some refractory HEAs (RHEAs) with single-phase body-centered cubic (BCC) crystal structure, e.g., TaNbMoW, TaNbMoWV and TiZrNbHfTa have exhibited improved strength and outstanding high temperature stability [15–18]. Among them, the TiZrNbHfTa RHEA shows a high room-temperature tensile strength of 1200 MPa with reasonably high ductility [18,19], moreover, it still maintains a single BCC structure without oxidation or forming new phase after annealing in vacuum at $1000~^{\circ}\text{C}$ for 2 h [20]. In addition, the eutectic AlCoCrFeNi $_{2.1}$ HEA with mixed FCC and BCC solid solution structure shows a tensile strength higher than 1 GPa and a ductility greater than 10% after thermo-mechanical processing [21,22]. The properties of the eutectic

^{*} Corresponding author. School of Materials Science and Engineering, Dalian University of Technology, Dalian, 116024, China. *E-mail address:* jiangli@dlut.edu.cn (L. Jiang).

alloy reflect a combination of the high strength of the BCC phase and high ductility of the FCC phase. Considering that different types of HEAs have a wide range of properties, exploring high entropy composites (HECs) could be a fruitful approach for developing advanced materials with unprecedented mechanical and physical properties.

Nanostructured metallic multilayers (NMMs) have been investigated due to promising applications in nuclear engineering [23–26], micro/nano-electromechanical devices [27], and optical systems [28]. The alternately stacked nano-layers in the NMMs provide material systems where the properties can be tuned by the size effect (layer thickness), crystal structures of the constituent layers, epitaxial matching and defect structure of interphase boundaries. The various crystal structure combinations of NMMs, such as FCC/FCC [29–31], BCC/BCC [32], FCC/HCP [33,34], and BCC/HCP [35] (hexagonal close packed) have demonstrated interesting characteristics compared to bulk metals. Especially, the FCC/BCC multilayers with discontinuous slip systems and interfaces that promote dislocation core spreading have been particularly effective as strong barriers to the transmission of dislocations [36–41].

In this work, high-entropy composite multilayers (HECMs) with alternating layers of CrMnFeCoNi and TiZrNbHfTa alloys were investigated to explore the synergistic effects of nanolayer and crystallinity on the strength and deformability of concentrated alloys. To study the size dependent behavior, HECMs with individual layer thickness of 5 and 50 nm were synthesized by magnetron sputtering. The microstructures were analyzed by transmission electron microscopy (TEM), and the mechanical properties were measured by nanoindentation. Deformation behavior was characterized by cross-section TEM and plan-view scanning electron microscopy (SEM) of nanoindents. Molecular Dynamics (MD) simulations were used to elucidate the deformation mechanisms.

2. Materials and methods

2.1. Sample preparation

The equiatomic CrMnFeCoNi and TiZrNbHfTa alloy targets were prepared at Oak Ridge National Lab by arc melting pure elemental metals (purity higher than 99.99 wt% and 99.9 wt%, respectively) in high-purity argon atmosphere. To facilitate mixing of the constituent elements, each ingot was flipped and re-melted five times and then allowed to solidify in a pancake-shaped water-cooled Cu mold. The cast ingots were homogenized in vacuum at 1200 °C for 48 h, sliced along the mid-plane by electric discharge machining, and ground until all the solidification shrinkage in the middle of the casting disappeared. After grinding, disk-shaped sputtering targets with diameter of 50.8 mm and height of 6.35 mm were obtained. The surface of the alloy targets was polished to mirror finish and ultrasonically cleaned in an ethanol bath to remove potential contamination from handling before insertion into the sputtering chamber.

Direct current (DC) magnetron sputtering was used to prepare HECM films from the alloy targets. The substrate for deposition was pure Si with a native SiO2 layer; it was ultrasonically cleaned in ethanol prior to deposition. The chamber was evacuated to 3.6×10^{-6} Pa before deposition and then maintained at 1 Pa by ventilating with argon during deposition. The sputtering power applied to the TiZrNbHfTa and CrMnFeCoNi targets was 150 and 116 W, respectively. The nominal deposition rate was 1.851 Å s⁻¹. To prepare the CrMnFeCoNi and TiZrNbHfTa single films, the corresponding single alloy target was used for continuous sputtering. In the case of the TiZrNbHfTa film which consists of higher melting elements, a periodic sputtering process was performed with a 30 min cooldown time after every 100 nm deposition, to avoid temperature increase of the substrate during continuous deposition. For the CrMnFeCoNi/TiZrNbHfTa HECMs (denoted below as C layer, and T layer, respectively) with individual layer thickness of 5 and 50 nm, sequential sputtering with the two alloy targets was conducted using an appropriate shutter system. All films were deposited on

the substrate nominally at room temperature to a total film thickness of 1 $\mu m.$

2.2. Microstructure and mechanical properties

Cross-sectional TEM samples were lifted out using dual-beam focused ion beam (FIB) technique on a FEI Helios Nanolab 650 working station. The microstructures were observed using a double Cs-corrected microscope (JEOL 3100R05) operated at 300 kV in a scanning TEM (STEM) mode. Composition analysis was performed using an analytical TEM (Talos F200X) equipped with four energy dispersive spectroscopy (EDS) detectors.

The hardness was measured by a Bruker Hysitron TI950 Triboindenter system equipped with a Berkovich tip, at a constant strain rate of $0.1\%~\rm s^{-1}$. The maximum penetration depth was set as 100 nm, i. e., 1/10 of the film thickness to avoid the substrate effect. Measurements were conducted at 10 or more different locations on each sample from which average values and standard deviations were determined. To further investigate the deformation mechanisms of the multilayers, the nanoindentation with 800 nm penetration depth was carried out on the surface of the 5 and 50 nm multilayers, and the surface morphologies of the indent were explored by scanning electron microscope (FEI Helios 650), while the microstructures of the cross sections through the indents were analyzed by TEM.

2.3. Molecular dynamics simulations

To elucidate the HECMs' deformation mechanisms, three types of models in atomistic simulations were set up and compared: Type-I, homogeneous amorphous T layer – crystalline C layer; Type-II, heterogeneous amorphous T layer – homogeneous amorphous C layer; and Type-III, heterogeneous amorphous T layer – crystalline C layer, respectively. The homogeneous amorphous layer represents a regular glassy structure, while the heterogeneous amorphous layer represents a density-fluctuating nano-granular structure retrieved from the experiments.

The tensile tests and deformation behaviors of the three models under the strain rate of 10⁷ s⁻¹ at 300 K were investigated by MD simulations using the LAMMPS software. The periodic boundary conditions were assigned to the y- (interfacial normal) and z- (perpendicular to screen) directions, while the free boundary condition was employed along the x-direction. The simulations were performed at 300 K with NPT (P = 0) control, and each tensile test contained a total time step of 2.5×10^7 at individual time step of 2 fs. The ratio between height (ydirection) and length (x-direction) was set to be around 2, in accordance with the experiments. The tensile loading is along the y direction. Admittedly, there is a considerable time scale gap between MD simulations and real experiments. Under some circumstances, such a strain rate mismatch would not change the deformation mechanisms but may lead to a quantitative yield strength variation [42-44], while under some special cases, it might trigger distinct deformation mechanisms [45,46]. We believe that in the scope of nanoindentation process the high strain rate in MD simulations would not significantly compromise the true physics underpinning because the indentation velocities in our simulations (~0.2 m/s) are far below the speed of sound, which indicates that MD simulations could effectively dissipate reflected waves due to the motion of the indenter and would not invoke a fundamentally different physical picture from the experiments [47]. In other earlier studies on the interface-mediated deformation in nano-structured materials, it was also demonstrated that the high strain rate in MD simulations did not affect the underlying interface physics [48]. Therefore, we believe the high simulation strain rate would not be a significant issue in the present study. We also examined different sizes of simulation cells ranging from 50,000 to 880,000 atoms, and no remarkable size or image force effects were observed. All the obtained data from MD simulations were displayed through "The Open Visualization Tool" (OVITO) [49].

It should be noted, describing the HECMs completely via atomistic simulations is challenging since it would require a high-fidelity interatomic potential capable of handling the collective particle interactions up to 10 different elements, which to our awareness, is not available to date. While one can always define some generic Lenard-Jones force fields or special bonding connections [50,51]to approximate the interactions between dissimilar atoms, the overwhelming parameters needed to fit a 10-element force field may inevitably compromise the predictive power of the modeling. Considering this, some simplifications have been made in the simulations, particularly for the TiZrNbHfTa layer that demonstrated amorphous structure. For CoCrFeMnNi, a reliable, modified embedded atom method (MEAM) inter-atomic potential was employed [52]. In the experiments reported in this manuscript, the HECM samples at 50 nm thickness exhibited crystalline structures in the C layer, where the lattice distortions caused by different species are postulated to influence the deformation behavior. Thus, it was important that the simulated Clayer captured the compositional complexity of 5 equimolar elements. As for the T layer, some flexibilities can be allowed because all the HECM samples in the present study exhibited amorphous structures, meaning that the lattice distortions in crystalline HEA phases may not be relevant in room temperature sputtered TiZrNbHfTa. In other words, it is not necessary to study the exact composition of TiZrNbHfTa; instead, it can be acceptable to construct the T layer using fewer elements, as long as it can interact with the C layer effectively in a similar way. To be more specific, the simplification made in the present study is to construct amorphous Mn layer as the substitution for T layer, and the reasons are four-fold (1) The chemical test results (e.g. Fig. 5b below) clearly show a diffusing Mn's profile that stretches into the T layer, meaning it can interchange with other elements and at least can represent some features of T layer; (2) Electronegativity of constituent elements have been found to play critical roles in complex alloys' mechanical and thermodynamic properties [53]. Mn's Smith electronegativity is close to the average value of Ta, Nb, Hf, Zr, and Ti elements [54,55], which suggests that it may be representative of some key features of T layer; (3) Using a single element with a similar valence electron concentration to represent a 5-element HEA has been practiced in the atomistic simulation and achieved consistent results with experimental observations [56]; (4) With such set up, one can directly employ the widely adopted force field for CrMnFeCoNi alloys [52] without the necessity of invoking further parameters or fittings.

3. Results

3.1. Microstructures

3.1.1. Microstructure of the as-deposited TiZrNbHfTa film

The cross-sectional TEM image of the TiZrNbHfTa film, Fig. 1a, shows different structure in the bottom 300 nm as compared to the top 700 nm. Columnar grains with 100 nm in width and BCC crystal structure are observed in the top layer, as shown in Fig. 1b and c, with no obvious texture detected. The amorphous nature of the bottom layer is confirmed by TEM, as shown in Fig. 1d and e, while isolated, faint diffraction spots in the selected area diffraction pattern (SADP) indicate the presence of a small amount of nanocrystals. The high resolution (HR) TEM image demonstrates a nanoscale granular amorphous morphology with dark and light contrasts, which is different from the typical glassy metals that exhibit maze-like contrast without any visible heterogeneities. The light cells are circled in orange in Fig. 1e, with an average cell size of 2-4 nm, while the inter-granular area with dark contrast shows an average spacing of around 1.5 nm. A similar microstructure called nanograined metallic glass (NGMG) [57,58] or nanoglass (NG) [59-67] has been reported in recent years. Typically, the granular morphology was

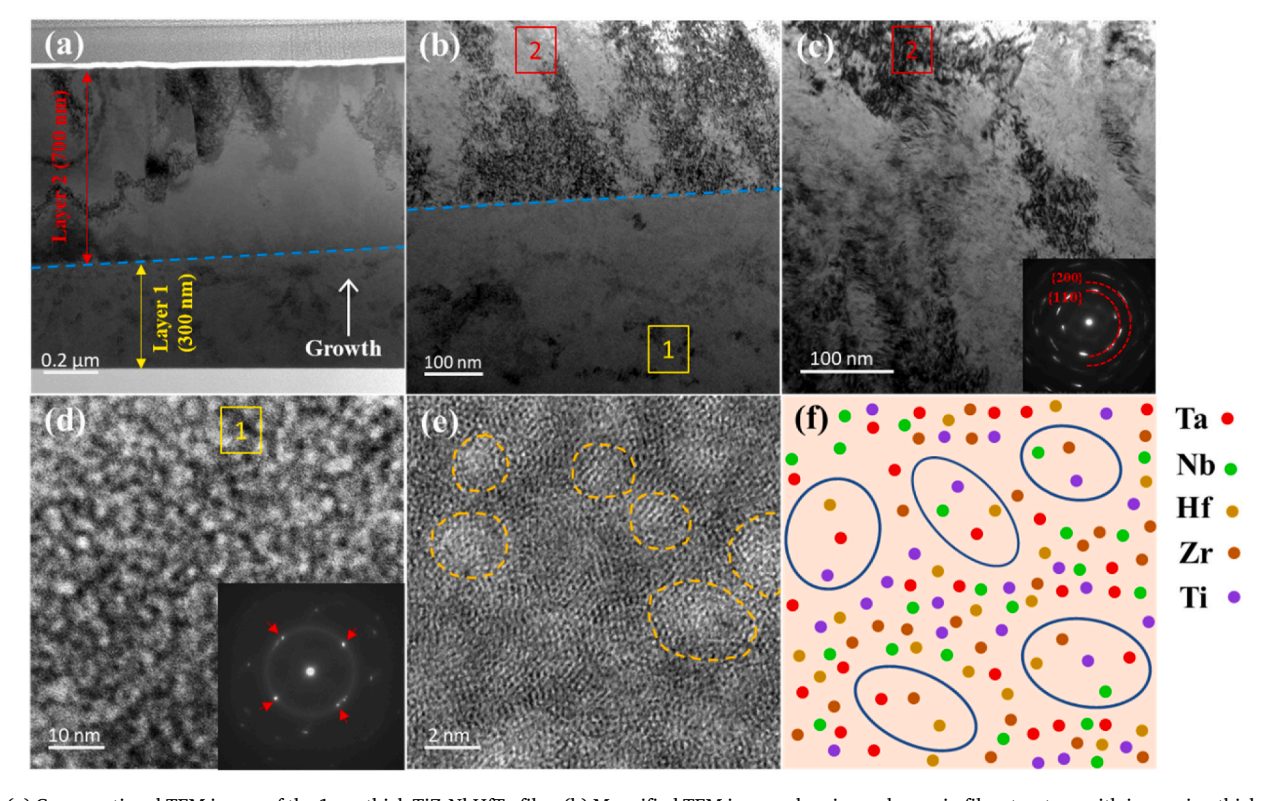


Fig. 1. (a) Cross-sectional TEM image of the 1 μ m thick TiZrNbHfTa film. (b) Magnified TEM image, showing a change in film structure with increasing thickness. (c) Microstructure and corresponding SADP of the top region (labeled as layer 2 in (a)), showing its polycrystalline structure. (d) Microstructure and corresponding SADP of the bottom region (labeled as layer 1 in (a)), showing its amorphous structure. (e) HRTEM image of the amorphous region, displaying the nanoscale granular amorphous morphology with amorphous cells, some of which are outlined by the dotted orange lines as a guide to the eye. (f) Schematic diagram of a granular amorphous structure showing regions of high and low relative density. (For interpretation of the references to color in this figure legend, the reader is referred to the Web version of this article.)

not induced by elemental segregation, while the dark area was believed to correspond to an amorphous region with high atomic density, and the light area with low atomic density [68]. A schematic diagram of the atomic arrangement for the granular amorphous structure is shown in Fig. 1f.

The nanocrystalline(top)/amorphous(bottom) structure in the TiZrNbHfTa film is quite different from the single-phase BCC crystal structure in its bulk, as-cast state [69]. In another investigation, thin films of TiZrNbHfTa that were DC magnetron sputtered at room temperature exhibited complete amorphous structure without a clear transition from amorphous to nanocrystalline with increasing film thickness [70]. For a similar composition of HfNbTiVZr (V instead of Ta), also a BCC structure was reported only in films deposited at 275 °C and the room temperature deposited films were amorphous [71]. During sputter deposition, the high quenching rate from vapor to solid limits the time available for diffusion in refractory HEAs, and thus the ability to form crystalline phases, leading to the amorphous microstructure. Non-equilibrium phases have also been reported in sputter deposited stainless steel thin films [72], but not the transition from amorphous to crystalline with increasing film thickness. In this study, an interrupted deposition of TiZrNbHfTa film was performed in which 30 min of cooldown time was inserted after every 100 nm of deposition, to minimize any temperature increase that may occur during continuous deposition. However, as can be seen in the bright field (BF) and high angle annular dark field (HAADF) cross-sectional TEM images in Fig. 2a and b, nanocrystalline (top)/amorphous (bottom) morphology again appears in this film. As before, the bottom layer with thickness of 300 nm is amorphous (Fig. 2c), while the top layer is polycrystalline with columnar grains. It seems that the columnar nanocrystalline structure is not caused by potential substrate heating during continuous deposition. Rather, a graded structure evolves gradually with increasing thickness with the bottom region predominantly amorphous containing dispersed nanocrystallites that seed the crystalline growth in the top region. Once critical size crystalline are nucleated, these tend to grow preferentially resulting in a columnar morphology.

3.1.2. Microstructure of the as-deposited CrMnFeCoNi film

The cross-sectional TEM image of the CrMnFeCoNi HEA film is shown in Fig. 3a where the nanoscale columnar crystals with grain boundaries perpendicular to the substrate are observed. Measurements of approximately 100 grains indicate that the average width of the columnar grains is 38 ± 2 nm. The inserted SADP not only suggests a single FCC crystal structure in the columnar grains with preferred orientation of [111], but also indicates the existence of nanotwins in the grain interior. Furthermore, the microstructure that is presented in Fig. 3b illustrates an ultrahigh density of nanotwins with interfaces parallel to the surface of the film. Fig. 3c and d shows the HRTEM images taken in the grain interior, in which the nanotwins and stacking faults

(SFs) with spacing ranging from 0.5 to 3 nm can be clearly observed. An amorphous substrate layer of \approx 300 nm thickness as reported in Ref. [73] for sputtered CoCrFeMnNi films was not observed in this study.

3.1.3. Microstructure of the as-deposited CrMnFeCoNi/TiZrNbHfTa 50 nm multilayer

Fig. 4a shows the cross-sectional microstructure of the CrMnFeCoNi/ TiZrNbHfTa 50 nm multilayer, with sharp and nominally flat interfaces. From the inserted SADP, both a diffuse halo and FCC diffraction spots are observed, indicating the coexistence of the amorphous structure and the FCC crystal structure in the multilayer. The magnified microstructure in Fig. 4b, illustrates an amorphous structure in the TiZrNbHfTa layer, and an FCC polycrystalline structure with SFs and nanotwins distributed along various orientations in the CrMnFeCoNi layer. From the [110] zone axis of the FCC phase, an ultrahigh density of nanotwins with (111) twinning plane perpendicular to the layer interface is observed in Fig. 4c (the magnified image of the blue framed area in Fig. 4b). However, in Fig. 4d, the magnified microstructure of the pink framed area in Fig. 4b, the (111) twinning plane nearly parallel to the layer interface is observed. The HRTEM image from the [111] zone axis in Fig. 4e, taken from the green framed area in Fig. 4b, further confirms the FCC structure in the CrMnFeCoNi layer. The HRTEM image in Fig. 4f taken from the TiZrNbHfTa layer (orange framed area in Fig. 4b) shows a heterogeneous amorphous structure. In addition, the elemental distribution of the CrMnFeCoNi/TiZrNbHfTa 50 nm multilayer was measured by EDS, and the resulting elemental maps are shown in Fig. 4g, illustrating a homogeneous distribution without segregation or clustering in both CrMnFeCoNi and TiZrNbHfTa layers.

3.1.4. Microstructure of the as-deposited CrMnFeCoNi/TiZrNbHfTa $5\ nm$ multilayer

The CrMnFeCoNi/TiZrNbHfTa 5 nm multilayer exhibits a high deposition quality, with each layer flat and their interfaces sharp, as can be seen in the cross-sectional TEM image in Fig. 5a. The corresponding SADP with fully diffuse halo shown in the insert suggests a completely amorphous structure in both T and C layers. The TiZrNbHfTa layer is amorphous in both 5 nm and 50 nm layer thickness samples. However, the CrMnFeCoNi layer is amorphous in the 5 nm layer thickness HECM, but crystalline structure in the 50 nm thickness HECM.

Similar to the 50 nm layer thickness case, all elements are distributed homogeneously in the 5 nm layers without the formation of any detectable solute clusters, as can be seen in the EDS results in Fig. 5b. From the magnified HAADF and BF TEM images in Fig. 5c,d, a typical maze-like amorphous structure is observed in the CrMnFeCoNi layer, while a nanoscale granular amorphous structure with dark and light contrast that mentioned in 3.1.1 is observed in the TiZrNbHfTa layer. The HRTEM images of T and C layers in Fig. 5e and f further confirm their amorphous nature. Together with the EDS results, it can be

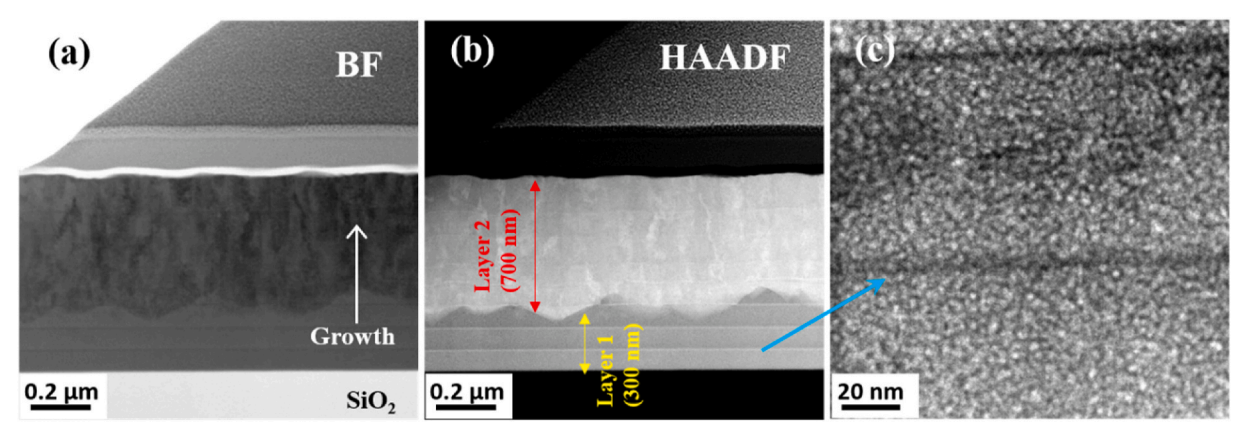


Fig. 2. Cross-sectional TEM images of the periodically deposited TiZrNbHfTa film: (a) BF. (b) HAADF. (c) Magnified TEM image of the bottom amorphous area.

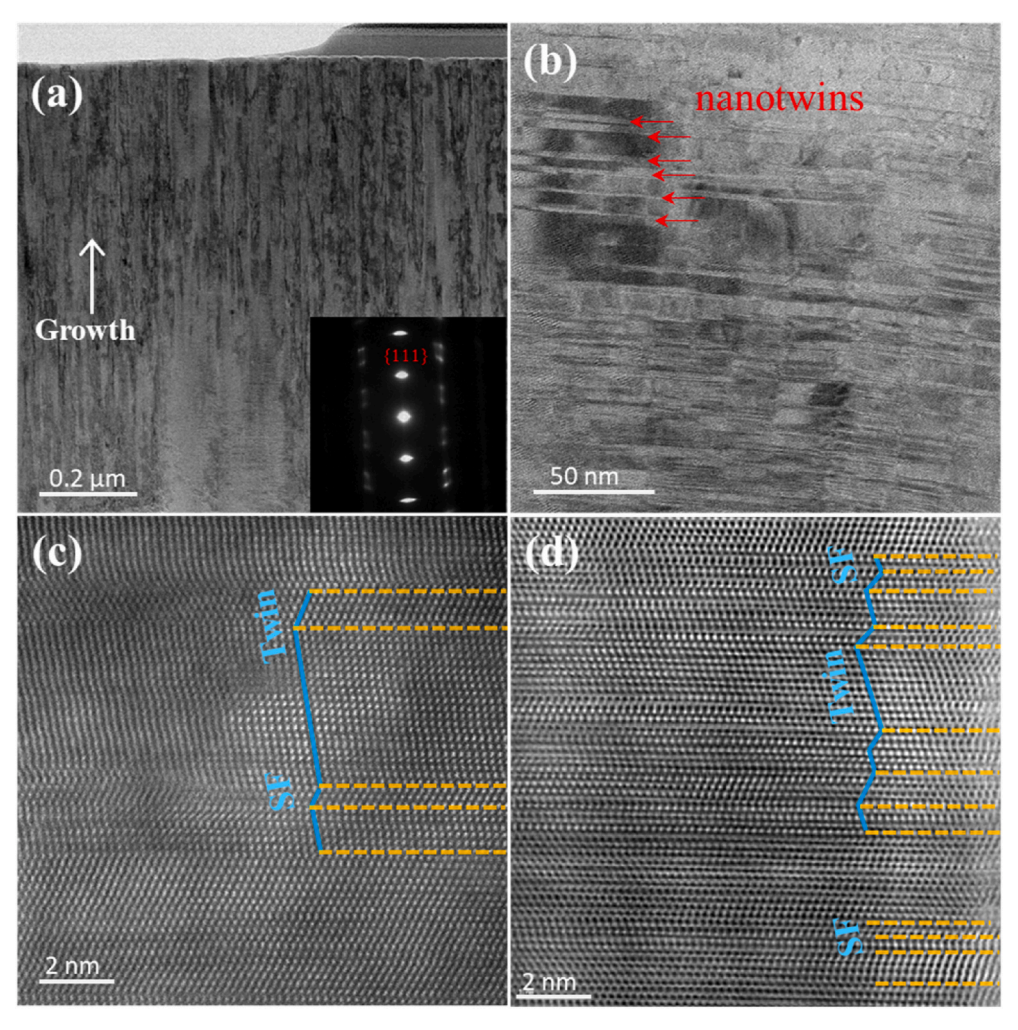


Fig. 3. (a) Cross-sectional TEM image of the CrMnFeCoNi film, and the corresponding SADP. (b) Magnified TEM image, showing a high density of planar defects in the film, the representative nanotwins are indicated by red arrows. (c,d) HRTEM images taken from the grain interior, displaying the nanotwins and stacking faults with spacing ranging from 0.5 to 3 nm. (For interpretation of the references to color in this figure legend, the reader is referred to the Web version of this article.)

concluded that the dark and light contrast is not induced by any elemental segregation, which has been reported in Ref. 68.

3.2. Mechanical properties

To evaluate the mechanical properties, nanoindentation tests were performed on the CrMnFeCoNi and TiZrNbHfTa single layer films as well as their 5 and 50 nm HECMs, and the representative load-depth profiles are shown in Fig. 6a. The CrMnFeCoNi film exhibits a hardness of 7.6 GPa which is attributed to the high density of nanotwins that effectively impede dislocation motion. The TiZrNbHfTa films prepared by continuous deposition (Fig. 1) and interrupted deposition (Fig. 2) show comparable hardness values given their similar microstructures. For the alloys with the same composition of TiZrNbHfTa, the film with layered amorphous and crystalline structures shows hardness of 6.1 GPa, which is superior to 4.9 GPa reported for bulk alloy with large grains [74], and lower than 12.5 GPa reported for sputtered thin film of TiZrNbHfTa alloy with fully amorphous structure [75]. For a similar HfNbTiVZr (V instead of Ta) sputtered thin film [71], hardness of the fully amorphous film was 6.5 GPa, increasing to 7.9 GPa for BCC nanocrystalline film and to 9.2 GPa with Laves phase precipitates in the BCC matrix. In Ref. [75], microstructure of the film was not reported, hence, it is not clear what caused the unusually high reported value of 12.5 GPa. For the TiZrNbHfTa film reported here, the top 70% of the film thickness is columnar nanocrystalline and hence, the indentation is

primarily measuring the deformation of the nanocrystalline region, although the measurement is likely affected by the bottom 30% region that is amorphous. The indentation results for TiZrNbHfTa film reported here in comparison with the literature [71] suggest that the film hardness can be controlled by the ratio of the amorphous to the crystalline structure.

The morphologies of the Berkovich indents on the 5 and 50 nm composite multilayer surfaces were investigated to compare the deformation behaviors, as shown in Fig. 6c and d. Both the indents exhibit a convexity at the edges of the equilateral triangle, suggesting pile-up at the contact surface during indentation. Well-developed circular deformation lines are observed at the edge of the indent of the 5 nm multilayer, as indicated by the blue dotted lines in Fig. 6c. Generally, the occurrence of shear bands inside the materials will leave protuberances on the sample surface, therefore, the high density of such loops around the indent indicates significant shear deformation in the 5 nm multilayer. However, from Fig. 6d, the irregular wave lines surrounding the indent of the 50 nm multilayer suggest a lower density of shear bands.

As for the CrMnFeCoNi/TiZrNbHfTa HECMs, the combination of the two amorphous structures in the 5 nm multilayer contributes to the high hardness of 7.8 GPa, while the combination of the amorphous structure and the crystalline structure with ultrahigh density of nanotwins in the 50 nm multilayer shows a lower but still high hardness of 5.6 GPa. This is not surprising because, compared with the crystalline C layer in the 50 nm sample, the amorphization of C layer in the 5 nm sample would

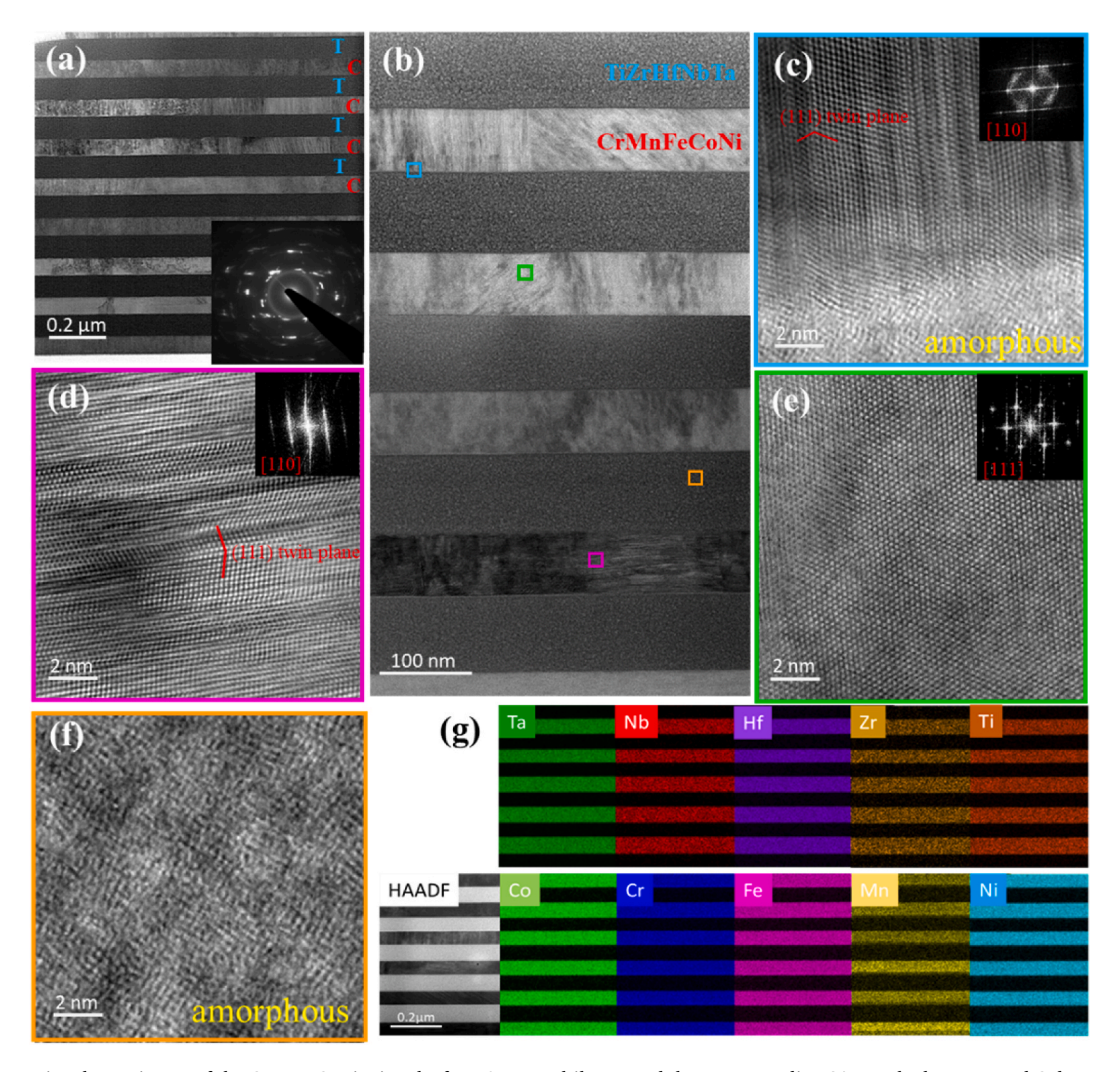


Fig. 4. (a) Cross-sectional TEM image of the CrMnFeCoNi/TiZrNbHfTa 50 nm multilayer, and the corresponding SADP. The letters T and C denote TiZrNbHfTa and CrMnFeCoNi layer, respectively. (b) Magnified TEM image, showing the FCC structure in the CrMnFeCoNi layer and the amorphous structure in the TiZrNbHfTa layer. (c,d) HRTEM images taken from [110] zone axis of FCC, displaying the twinning plane perpendicular and parallel to the layer interface, respectively. (e) HRTEM image taken from [111] zone axis of FCC. (f) HRTEM image taken from TiZrNbHfTa layer, showing a heterogeneous amorphous structure. (g) EDS results of the 50 nm multilayer.

make plastic strain more difficult to propagate and thus yield a higher strength.

4. Discussion

Fig. 7a below shows the stress-strain curves for all 3 types of models in atomistic simulations. The retrieved Young's modulus is around 70 GPa, which is close to experimental results. Among the 3 curves, the sample with amorphized C-layer (i.e. Type-II) exhibits the highest strength around 2.2 GPa; while the samples with crystalline C-layer (i.e. Type-I and Type-III) exhibit a lower strength around 1.5–1.7 GPa. Note that these numbers are the uniaxial tensile strength values in simulations, and they are reasonably well consistent with the indentation measurements considering the hardness to flow strength conversion factor of around 3 or slightly above.

To better demonstrate the role of C-layer in HECMs, we compared the deformation mechanisms between Type-II and Type-III models, where they possess the same T layer (heterogeneous amorphous structure) while having different C layers (homogeneous amorphous for Type-II and crystalline for Type-III). It is observed that under the same loading conditions, the Type-III's C layer exhibits more extended shear deformation than Type-II does. For example, as seen in Fig. 7b, at the global tensile strain of 0.08 the shear strain of C layer in Type-III already

propagates across the sample, while in Type-II it is still highly localized near the C/T interface. As mentioned above in Sec. 2.3, no significant size effect has been observed in simulations in terms of the tensile strength and deformation mechanism. This indicates the amorphization of C-layer is the main factor that further strengthens the HECMs, corroborating the experimental measurements.

It is worth emphasizing that, both these values of hardness are superior to those of previous multilayers with the same thickness, such as 5.5 and 4.8 GPa, respectively, for the Cu/Ta multilayers with thickness of 5 and 50 nm [76] and 6.4 and 4.3 GPa, respectively, for the Cu/Nb multilayers with thickness of 5 and 50 nm [38]. Moreover, the hardness is even higher than the values, 6.8 and 4.9 GPa for Cu/(Ta50Nb25Mo25) 5 and 50 nm multilayers [77]. Therefore, the present CrMnFeCoNi/TiZrNbHfTa HECMs exhibit potential for achieving higher hardness than FCC/BCC elemental multilayers.

In order to experimentally characterize the deformation mechanisms of the 5 and 50 nm HECM, the cross-sections of the indents with a total indentation depth of 800 nm were lifted out by FIB and studied by TEM. For the cross-section through the indent in the 5 nm multilayer (Fig. 8a), a series of shear bands is observed, indicating the localized shear deformation in the film. The magnified TEM image in Fig. 8b suggests that the shear deformation has triggered the instability of the interface, resulting in thinner and blurrier layer-interfaces in the shear bands. The

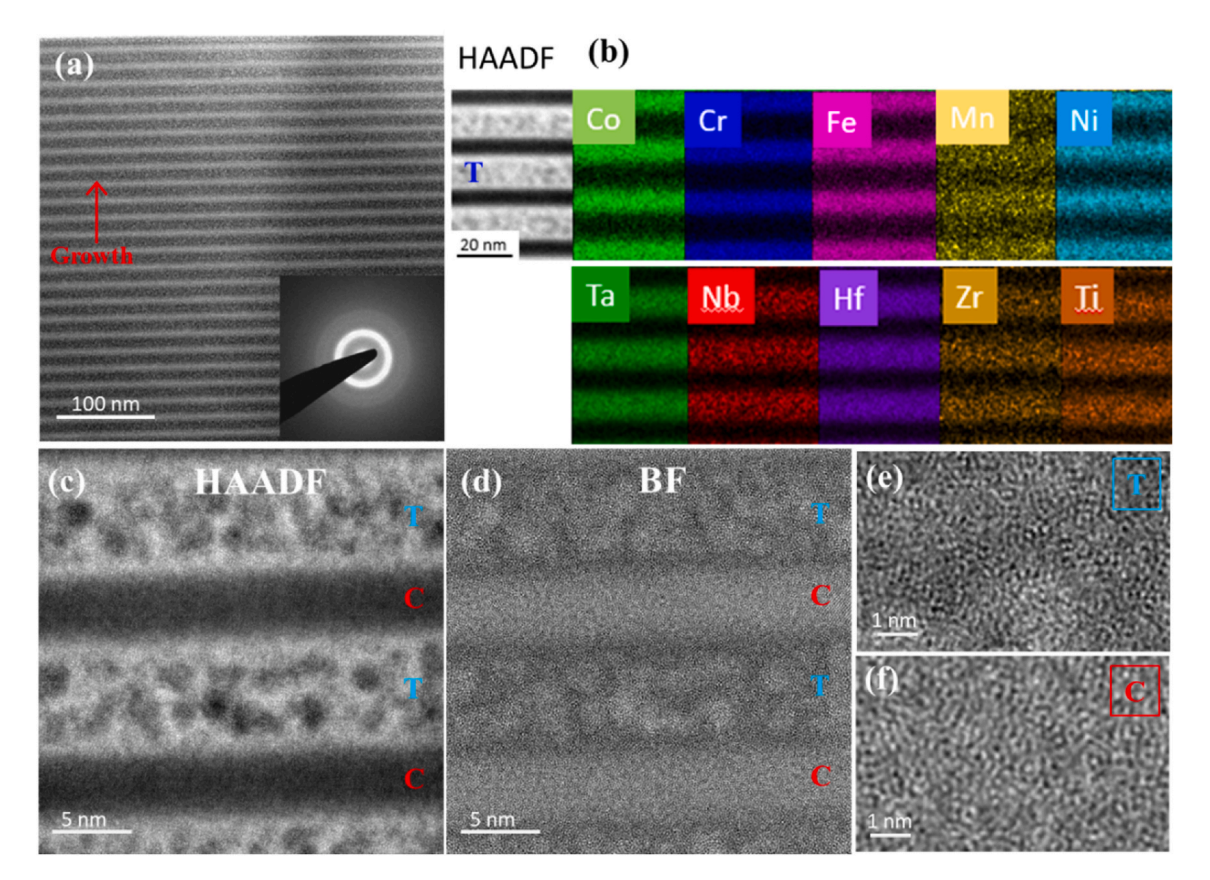


Fig. 5. (a) Cross-sectional TEM image of the CrMnFeCoNi/TiZrNbHfTa 5 nm multilayer, and the corresponding SADP. (b) EDS results of the 5 nm multilayer. (c,d) HAADF and BF TEM images, showing the maze-like amorphous structure and nanoscale granular amorphous structure in the CrMnFeCoNi and TiZrNbHfTa layers, respectively. The letters T and C denote TiZrNbHfTa and CrMnFeCoNi layers, respectively. (e,f) HRTEM images of the granular and maze-like amorphous structures in T and C layer, respectively.

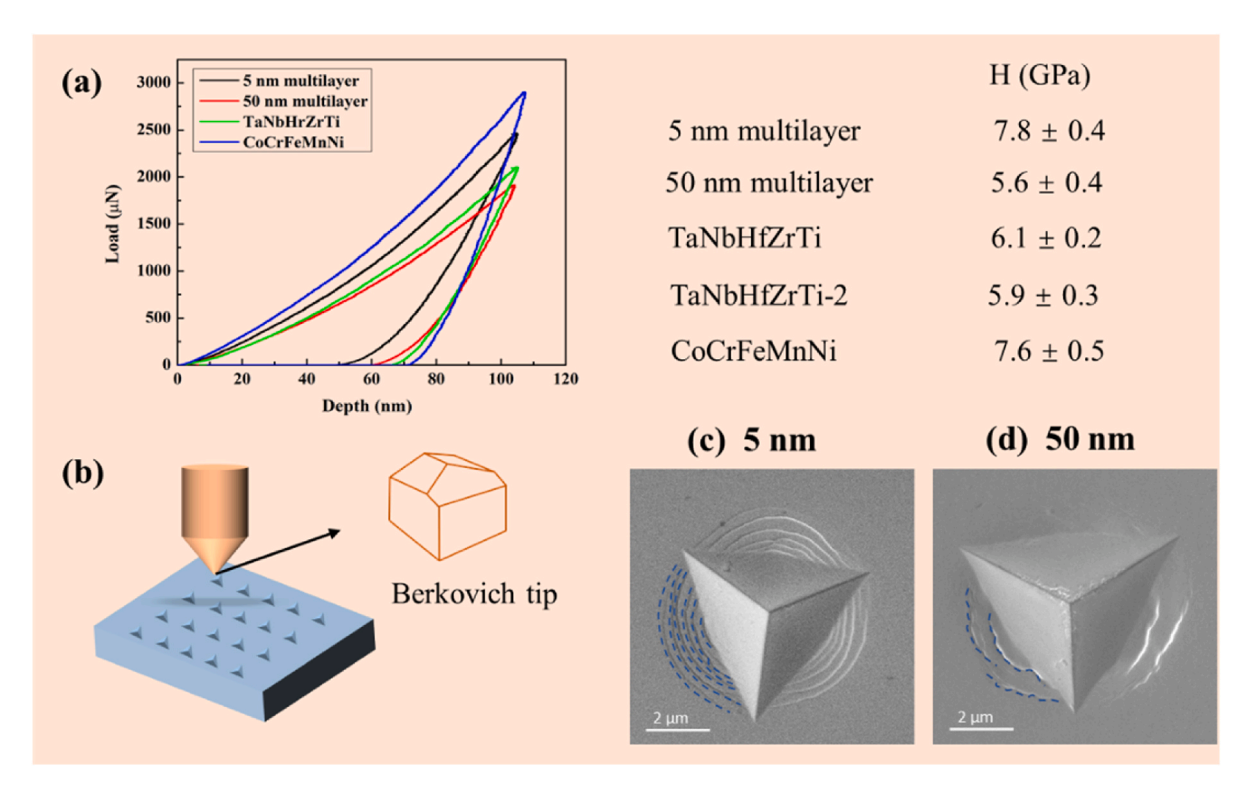


Fig. 6. (a) Representative load-depth curves of the 5 and 50 nm HECMs and TiTaHfNbZr and CrMnFeCoNi single films, in which the periodically deposited TiTaHfNbZr film is denoted as TiZrNbHfTa-2. (b) Schematic diagram of the Berkovich tip. (c,d) SEM images of the indent surface of the 5 and 50 nm multilayers, respectively.

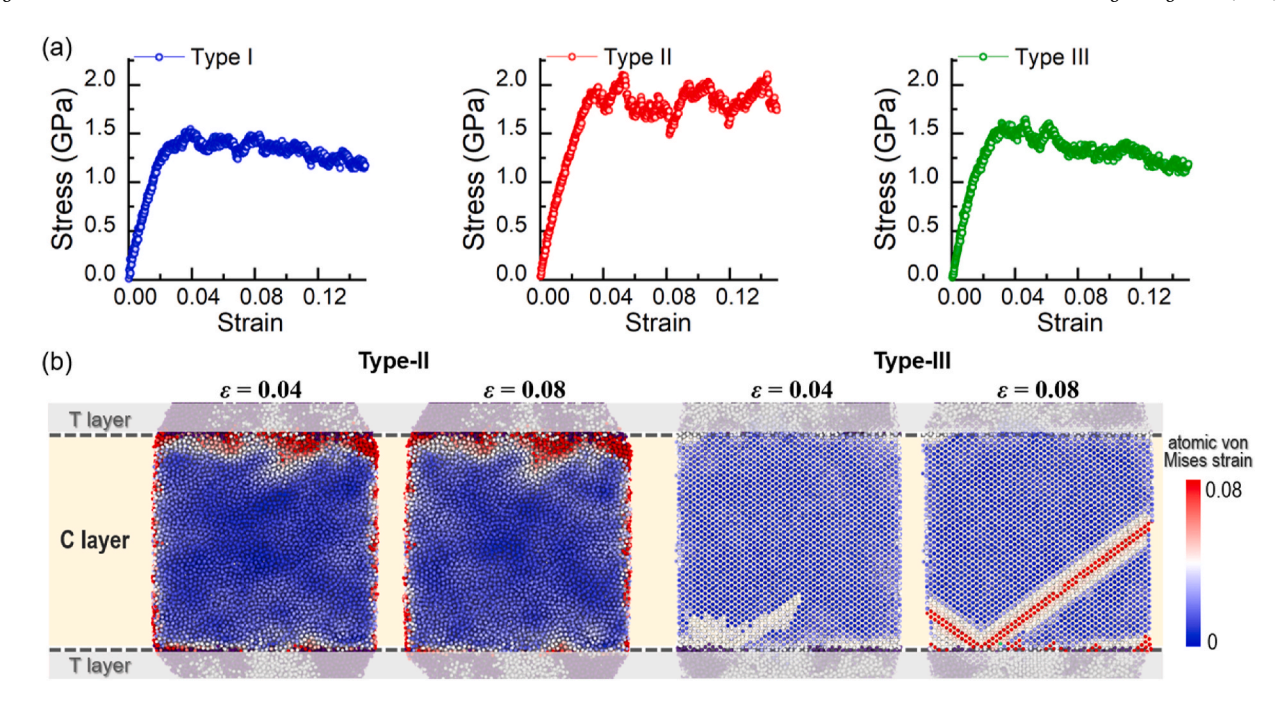


Fig. 7. (a) The tensile loading along the y direction is applied and stress-strain curves for all three types of models in atomistic simulations. (b) Deformation behaviors in Type-II and Type-III models under uniaxial loading. Type-II consists of heterogeneous amorphous T (TiZrNbHfTa) layer and homogeneous amorphous C (CrMnFeCoNi) layer, while Type-III consists of heterogeneous amorphous T layer and crystalline C layer. It is clear that the C layer with FCC crystal structure in Type-III exhibits more extended shear deformation than in that with homogeneous amorphous structure in Type-II under the same loading conditions. Note that to focus on the role of C layer in HECMs, here we only highlight the atomic level von Mises strain in C layers of both Type-II and Type-III. It is worth clarifying that, from the whole system level the plastic deformation is more likely to initiate and concentrate in T layers (see Fig. 9 below). When the C layer is amorphized, the shear deformation is more difficult to propagate through compared with the scenarios where C layer is in crystalline structure, and that is why Type-II presents the highest strength.

kink angle (ϕ) of the shear bands is about 45° , and the thickness of the shear bands ranges from 10 to 40 nm, comparable with those of the bulk amorphous alloys [78,79]. A close-up view of the shear band in Fig. 8c indicates a shearing displacement of 5 nm. Generally, the 5 nm multilayer exhibits a similar deformation behavior with that of most conventional amorphous alloys.

Fig. 8d shows the cross-sectional TEM image of the indent in the 50 nm multilayer, which demonstrates co-compression of the CrMnFeCoNi and TiZrNbHfTa layers at the right bottom of the indenter tip, with a wave-like layer buckling beside the indenter. This cooperative buckling and rotation of the constituent layers could further lead to a wide shear band [80–82]. To be noted, the curvature of the buckled layers along the shear banding direction decreases with increasing indentation depth. For the layers close to the surface, even the amorphous TiZrNbHfTa layers maintain continuity without fracture, although the shear displacement has exceeded several times the thickness of the individual layers, which suggests an excellent co-deformation of the constituent layers. However, for the layers close to the substrate, the localized shear deformation occurs in the TiZrNbHfTa layers due to the limited buckling under the control of the adjacent top layer. As the strain concentration cannot be released through layer buckling, it accumulates in a small region and finally induces the formation of a localized shear band. Meanwhile, the CrMnFeCoNi layers maintain an intact microstructure due to the release of the strain concentration by the internal ultrahigh density of SFs and nanotwins during deformation. From the magnified BF and HAADF images of the deformed microstructures in Fig. 8e, a nanoscale shear deformation with shearing displacement of about 30 nm is observed in the TiZrNbHfTa layer. A close-up view of the indented region revealed a reorientation and agglomeration of sheared amorphous zones along the shear band direction (Fig. 8f). Furthermore, these columnar amorphous zones or "grains" serve to provide channels for plastic flow during deformation, rather than strengthening the alloy by blocking or branching the shear band. As a result, the amorphous TiZrNbHfTa nanolayers exhibit good deformability compared to the conventional amorphous materials with limited plasticity [83,84]. Such a mechanism is also confirmed by atomistic simulations shown in Fig. 9, in which the deformation behaviors of the Type-I (homogeneous amorphous T layer - crystalline C layer) and Type-III (heterogeneous amorphous T layer - crystalline C layer) models under the same conditions are compared. Since C layers are identical in both models, the differences can only originate from T layers, namely the conventional homogeneous amorphous structure (Type-I) vs. the heterogeneous nano-granular amorphous structure (Type-III). It can be seen from Fig. 9a-c and e-g that the deformation behaviors in C layers are similar, namely the nucleation of SFs at C/T interfaces and the subsequent slip propagation. However, the deformation mechanisms in T layers are remarkably different. It is clear from Fig. 9d,h that the number of particles with high atomic-level shear strain is much larger in Type-III than in Type-I. Furthermore, those highly-strained regions are confined in a thin shear band in Type-I, while in Type-III, by contrast, additional plastic deformation channels show up. By scrutinizing the T layer's microstructural evolution through Fig. 9e-g, it is evident that the enhanced plasticity in Type-III is due to the reorientation and aggregation of nano-granules in the T layer, in accordance with the experimental results. Again, no significant size effect has been observed in simulations, and as long as the T layers are in heterogeneous nano-granular structures the system would present enhanced plasticity.

It is worth noting that similar softening phenomenon has been observed in most NGMGs, like Cu–Zr, Cu–Zr–Al and Zr–Cu–Al–Mo alloys [85–88]. Adibi et al. [89] reported an amorphous grain size (*d*) dependent deformation behavior in NGMGs using molecular dynamics simulation. Their results confirm that the deformation mode changes from shear fracture to plastic flow when *d* decreases from 15 to 5 nm. Therefore, the amorphous grains with size of 4 nm in this work could effectively improve the ductility of the amorphous alloys. In general, amorphous alloys are widely studied due to their high hardness and low

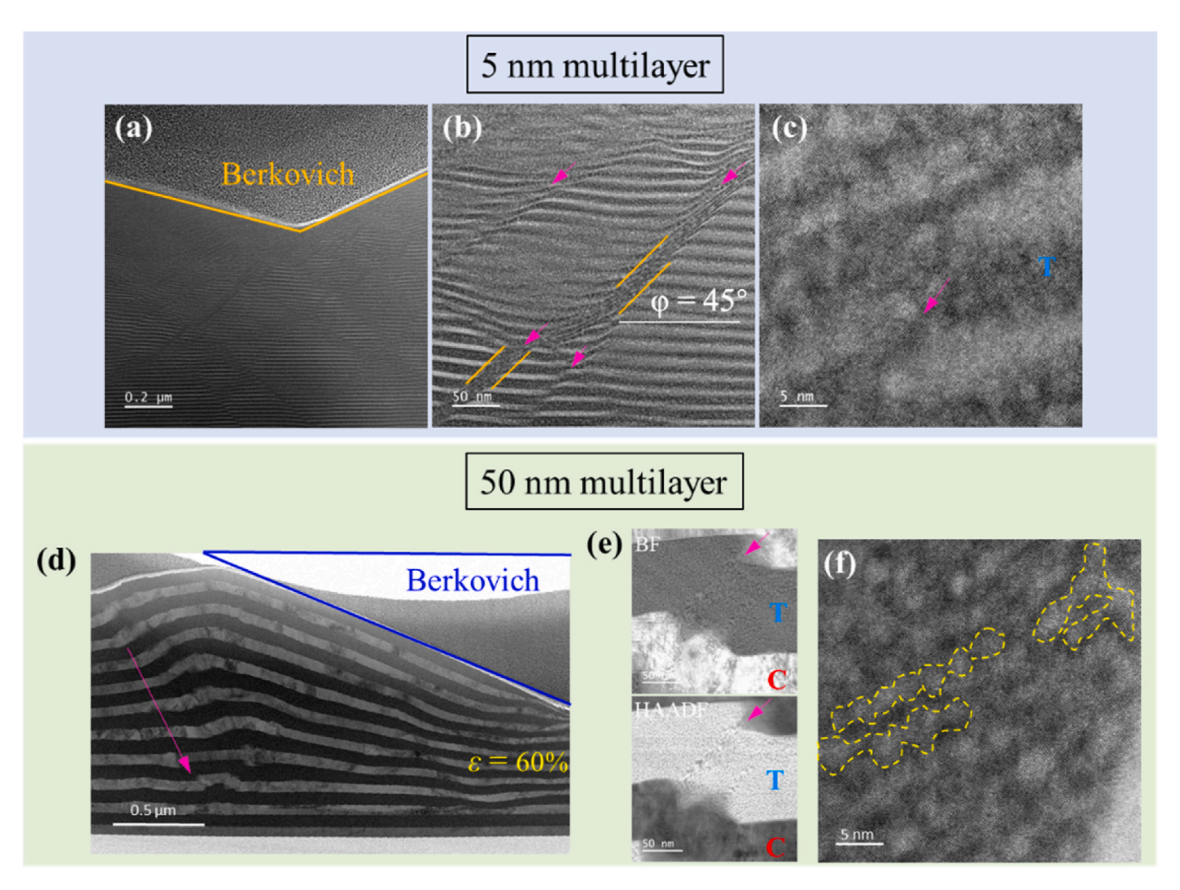


Fig. 8. (a) Cross-sectional TEM image of the indented region of the 5 nm multilayer. (b) TEM image of the deformed area, exhibiting shear bands. (c) A magnified TEM image, showing the details of the shear band. (d) Cross-sectional TEM image of the indented region of the 50 nm multilayer. (e) BF and corresponding HAADF images, indicating the shear deformation in the TiZrNbHfTa layer. (f) TEM image of the deformed TiZrNbHfTa layer, showing the amorphous cells agglomerate along the shear direction. The pink arrows in the figures indicate the shear deformation. (For interpretation of the references to color in this figure legend, the reader is referred to the Web version of this article.)

elastic modulus, but poor deformability limits their further application. A crystalline-amorphous nanocomposite with nanocrystalline grains containing high density of nanotwins wrapped by nanoscale amorphous regions was obtained by doping glass-forming elements into a crystalline CrCoFeNi system. It realized a near theoretical yield strength of 4.1 GPa and a homogeneous compressive strain of 45% [90]. During deformation, the crystalline part serves to improve the plasticity of the alloy through mechanically driven de-twinning, while the strain hardening from the amorphous part and the crystalline-amorphous interfaces effectively strengthens the alloy. Furthermore, a BCC phase embedded in the amorphous matrix [91], or a nano-multilayer mixed with crystalline and amorphous layers [92–94] are equally effective in improving the deformability by branching the shear bands and thus avoiding catastrophic shear fracture in the amorphous regions.

Finally, it is noted that hardness of the single phase CrMnFeCoNi film, 7.6 ± 0.5 GPa, was nearly equal to the hardness of the 5 nm HECM multilayer, 7.8 ± 0.4 GPa, although the hardening mechanisms are different. This is due to the nanocrystalline columnar morphology with 38 ± 2 nm average columnar width containing a high density of SFs and twin interfaces with spacing ranging from 0.5 to 3 nm in single phase CrMnFeCoNi film. In FCC metals, nanotwinned sputtered films have been shown to produce high hardness, approaching 6.5 GPa in austenitic stainless steel 330 [95] and tensile strength of ≈ 1.2 GPa in Cu [96]. The hardness of nanotwinned HEA film is significantly higher than that of nanotwinned austenitic stainless steel for comparable column size and twin spacing. It thus seems that for HEA systems, on one hand, it is easy to obtain crystalline/amorphous structures in sputtered thin films; on the other hand, its excellent properties combining the range of nanoscale structural dimensions, alloy compositions and structures provide

numerous possibilities for developing advanced materials with unprecedented mechanical and physical properties.

5. Conclusions

In this work, high-entropy composite multilayers based on the compositions of typical FCC-structured CrMnFeCoNi and BCC-structured TiZrNbHfTa were successfully synthesized by magnetron sputtering from two pre-alloyed sputtering targets. To investigate the size dependent microstructural evolution, the CrMnFeCoNi and TiZrNbHfTa single films and their corresponding composite multilayers with individual layer thickness of 5 and 50 nm were prepared.

Single phase FCC CrMnFeCoNi film exhibits nanotwinned structure with high hardness of $\approx\!7.6$ GPa even higher than the hardness of $\approx\!6.1$ GPa observed in the refractory TiZrNbHfTa film that exhibited an unusual gradient structure changing from nanocrystalline near film surface to amorphous/nano-glass near substrate.

The 50 nm high-entropy composite multilayers (HECM) with granular amorphous structure in the TiZrNbHfTa layers and FCC structure in the CrMnFeCoNi layers demonstrates simultaneously high hardness and deformability, taking full advantages of both phases. The novel mechanism of the reorientation and agglomeration of granular nano-glasses in the TiZrNbHfTa layer, which enables more plastic activities compared with conventional uniform-density amorphous solids, in conjunction with the nanotwinned structure in the CrMnFeCoNi layer, is the key to achieve high strength and plastic deformability in HECMs. On the other hand, hardness is maximized, although at loss of uniform plastic deformability, when nano-glass structure of the TiZrNbHfTa layer is combined with homogeneous glassy structure of CrMnFeCoNi

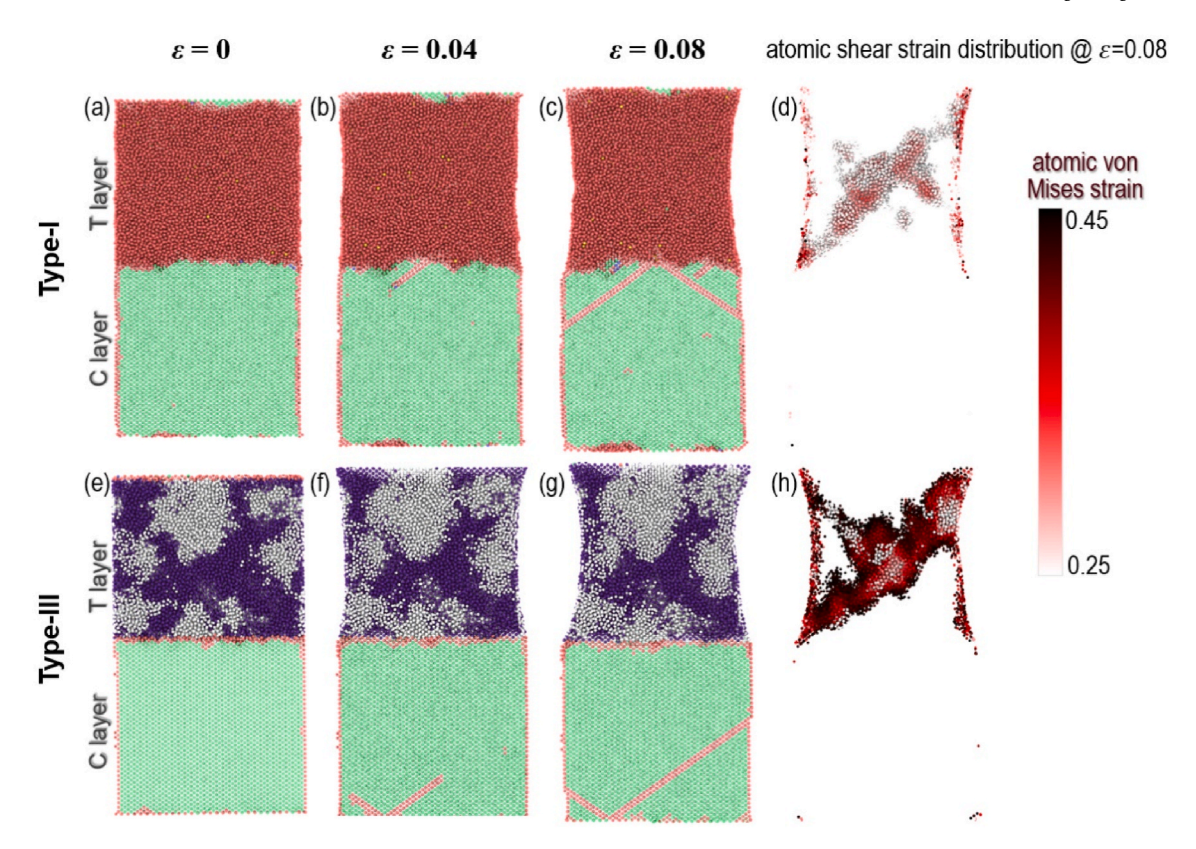


Fig. 9. Deformation behaviors in Type-I (homogeneous amorphous T layer – crystalline C layer) and Type-III (heterogeneous amorphous T layer – crystalline C layer) models under uniaxial loading. As discussed in the main text, Type-I consists of conventional amorphous T layer and crystalline C layer, while Type-III consists of heterogeneous amorphous T layer and crystalline C layer. The panels (a)–(c) are colored according to the common neighbor analysis, where green represents FCC environment and red represents non-FCC environment. The C layers in panels (e)–(g) are colored according to common neighbor analysis, while the T layers are colored according to the local density of the nano-granular structure, where purple represents high density region and grey represents low density region. Panels (d) and (h) display the distributions of the particles with larger atomic-level von Mises shear strain. (For interpretation of the references to color in this figure legend, the reader is referred to the Web version of this article.)

layer, resulting in high hardness of 7.8 GPa in the 5 nm layer thickness HECM.

High-entropy composite multilayers provide new opportunities to develop strong and plastically deformable structural materials through synergistic mechanisms involving size (nanolayer), structure (crystalline/nano-glass) and chemistry (multi-component concentrated alloys).

Notice of copyright

This manuscript has been co-authored by UT-Battelle, LLC under Contract No. DE-AC05-00OR22725 with the U.S. Department of Energy. The United States Government retains and the publisher, by accepting the article for publication, acknowledges that the United States Government retains a non-exclusive, paid-up, irrevocable, worldwide license to publish or reproduce the published form of this manuscript, or allow others to do so, for United States Government purposes. The Department of Energy will provide public access to these results of federally sponsored research in accordance with the DOE Public Access Plan (http://energy.gov/downloads/doe-public-access-plan).

CRediT authorship contribution statement

Li Jiang: conducted the TEM, Formal analysis, Writing – original draft. Zhitong Bai: conducted the simulations. Max Powers: performed sputter deposition of the multilayer samples, performed sputter deposition of the multilayer samples. Yue Fan: conducted the simulations, made significant improvement. Wei Zhang: provided discussion about the microstructures of amorphous multilayers. Easo P. George: provided the high-quality alloy targets for sputtering. Amit Misra:

Conceptualization, Methodology, finalized the manuscript.

Declaration of competing interest

The authors declare that they have no known competing financial interests or personal relationships that could have appeared to influence the work reported in this paper.

Acknowledgements

LJ acknowledge support from the National Natural Science Foundation of China (No. 52101036). MP and AM acknowledge support from the Center for Research Excellence on Dynamically Deformed Solids (CREDDS) sponsored by the Department of Energy-National Nuclear Security Administration (DOE-NNSA), Stewardship Science Academic Program under the Award No. DE-NA0003857. The authors acknowledge support from University of Michigan, and access to the Michigan Center for Materials Characterization. EPG is supported by the U.S. Department of Energy, Office of Science, Basic Energy Sciences, Materials Sciences and Engineering Division. ZB and YF's contribution is based upon work supported by the NSF DMR-1944879.

References

- B. Cantor, I.T.H. Chang, P. Knight, A.J.B. Vincent, Microstructural development in equiatomic multicomponent alloys, Mater. Sci. & Eng. A 375–377 (2004) 213–218.
- [2] J.W. Yeh, S.K. Chen, S.J. Lin, J.Y. Gan, T.S. Chin, T.T. Shun, C.H. Tsau, S.Y. Chang, Nanostructured high-entropy alloys with multiple principal elements: novel alloy design concepts and outcomes, Adv. Eng. Mater. 6 (2004) 299–303.

- [3] Q. Ding, Y. Zhang, X. Chen, X. Fu, D. Chen, S. Chen, L. Gu, F. Wei, H. Bei, Y. Gao, Tuning element distribution, structure and properties by composition in highentropy alloys, Nature 574 (2019) 223–227.
- [4] Z. Lei, X. Liu, Y. Wu, H. Wang, S. Jiang, S. Wang, X. Hui, Y. Wu, B. Gault, P. Kontis, Enhanced strength and ductility in a high-entropy alloy via ordered oxygen complexes, Nature 563 (2018) 546–550.
- [5] Z. Li, K.G. Pradeep, Y. Deng, D. Raabe, C.C. Tasan, Metastable high-entropy dualphase alloys overcome the strength-ductility trade-off, Nature 534 (2016) 227–230
- [6] B. Gludovatz, A. Hohenwarter, D. Catoor, E.H. Chang, E.P. George, R.O. Ritchie, A fracture-resistant high-entropy alloy for cryogenic applications, Science 345 (2014) 1153–1158
- [7] E. Ma, X. Wu, Tailoring heterogeneities in high-entropy alloys to promote strength-ductility synergy, Nat. Commun. 5623 (2019) 10.
- [8] P. Shi, W. Ren, T. Zheng, Z. Ren, X. Hou, J. Peng, P. Hu, Y. Gao, Y. Zhong, P. K. Liaw, Enhanced strength-ductility synergy in ultrafine-grained eutectic highentropy alloys by inheriting microstructural lamellae, Nat. Commun. 489 (2019) 10
- [9] W. Guo, J. Su, W. Lu, C.H. Liebscher, C. Kirchlechner, Y. Ikeda, F. Körmann, X. Liu, Y. Xue, G. Dehm, Dislocation-induced breakthrough of strength and ductility tradeoff in a non-equiatomic high-entropy alloy, Acta Mater 185 (2020) 45–54.
- [10] L. Jiang, Y.P. Lu, M. Song, C. Lu, K. Sun, Z.Q. Cao, T.M. Wang, F. Gao, L.M. Wang, A promising CoFeNi2V0.5Mo0.2 high entropy alloy with exceptional ductility, Scr. Mater. 165 (2019) 128–133.
- [11] L. Jiang, Y. Lu, Y. Dong, T. Wang, Z. Cao, T. Li, Annealing effects on the microstructure and properties of bulk high-entropy CoCrFeNiTi0.5 alloy casting ingot, Intermetallics 44 (201) 37-43.
- [12] L. Jiang, Y. Lu, W. Wu, Z. Cao, T. Li, Microstructure and mechanical properties of a CoFeNi2V0.5Nb0.75 eutectic high entropy alloy in as-cast and heat-treated conditions, J. Mater. Sci. Technol. 32 (2016) 245–250.
- [13] S.S. Nene, M. Frank, K. Liu, S. Sinha, R.S. Mishra, B.A. McWilliams, K.C. Cho, Corrosion-resistant high entropy alloy with high strength and ductility, Scr. Mater. 166 (2019) 168–172.
- [14] M. Chuang, M. Tsai, W. Wang, S. Lin, J.W. Yeh, Microstructure and wear behavior of AlxCo1.5CrFeNi1.5Tiy high-entropy alloys, Acta Mater 59 (2011) 6308–6317.
- [15] O.N. Senkov, G.B. Wilks, D.B. Miracle, C.P. Chuang, P.K. Liaw, Refractory highentropy alloys, Intermetallics 18 (2010) 1758–1765.
- [16] H. Kim, S. Nam, A. Roh, M. Son, M. Ham, J. Kim, H. Choi, Mechanical and electrical properties of NbMoTaW refractory high-entropy alloy thin films, Int. J. Refract. Hard. Met. 80 (2019) 286–291.
- [17] S. Alvi, D.M. Jarzabek, M.G. Kohan, D. Hedman, P. Jenczyk, M.M. Natile, A. Vomiero, F. Akhtar, Synthesis and mechanical characterization of a CuMoTaWV high-entropy film by magnetron sputtering, ACS Appl. Mater. Inter. 12 (2020) 21070–21079.
- [18] C. Juan, M. Tsai, C. Tsai, C. Lin, W. Wang, C. Yang, S. Chen, S. Lin, J.W. Yeh, Enhanced mechanical properties of HfMoTaTiZr and HfMoNbTaTiZr refractory high-entropy alloys, Intermetallics 62 (2015) 76–83.
- [19] M. Hu, W. Song, D. Duan, Y. Wu, Dynamic behavior and microstructure characterization of TaNbHfZrTi high-entropy alloy at a wide range of strain rates and temperatures, Int. J. Mech. Sci. 182 (2020), 105738.
- [20] O.N. Senkov, S.L. Semiatin, Microstructure and properties of a refractory highentropy alloy after cold working, J. Alloy. Compd. 649 (2015) 1110–1123.
- [21] I.S. Wani, T. Bhattacharjee, S. Sheikh, Y.P. Lu, S. Chatterjee, P.P. Bhattacharjee, S. Guo, N. Tsuji, Ultrafine-grained AlCoCrFeNi2.1 eutectic high- entropy alloy, Mater. Res. Lett. 4 (2016) 174–179.
- [22] I.S. Wani, T. Bhattacharjee, S. Sheikh, P.P. Bhattacharjee, S. Guo, N. Tsuji, Tailoring nanostructures and mechanical properties of AlCoCrFeNi2.1 eutectic high entropy alloy using thermo-mechanical processing, Mater. Sci. & Eng. A 675 (2016) 99–109.
- [23] X. Zhang, E.G. Fu, Nan Li, A. Misra, Y.Q. Wang, L. Shao, H. Wang, Design of Radiation Tolerant Nanostructured Metallic Multilayers 134 (4) (2012), 041010.
- [24] K.V. Manukyan, W. Tan, R.J. DeBoer, E.J. Stech, A. Aprahamian, M. Wiescher, S. Rouvimov, K.R. Overdeep, C.E. Shuck, T.P. Weihs, Irradiation-enhanced reactivity of multilayer Al/Ni nanomaterials, ACS Appl. Mater. Inter. 7 (2015) 11272–11279.
- [25] Q.M. Wei, N. Li, N. Mara, M. Nastasi, A. Misra, Suppression of irradiation hardening in nanoscale V/Ag multilayers, Acta Mater 59 (2011) 6331–6340.
- [26] Y. Chen, Y. Liu, E.G. Fu, C. Sun, K.Y. Yu, M. Song, J. Li, Y.Q. Wang, H. Wang, X. Zhang, Unusual size-dependent strengthening mechanisms in helium ionirradiated immiscible coherent Cu/Co nanolayers, Acta Mater 84 (2015) 393–404.
- [27] S.N. Piramanayagam, Perpendicular recording media for hard disk drives, J. Appl. Phys. 102 (2007) 11301.
- [28] S.A. Bogachev, N.I. Chkhalo, S.V. Kuzin, D.E. Pariev, V.N. Polkovnikov, N. N. Salashchenko, S.V. Shestov, S.Y. Zuev, Advanced materials for multilayer mirrors for extreme ultraviolet solar astronomy, Appl. Opt. 55 (2016) 2126–2135.
- [29] Y. Liu, D. Bufford, H. Wang, C. Sun, X. Zhang, Mechanical properties of highly textured Cu/Ni multilayers, Acta Mater 59 (2011) 1924–1933.
- [30] D. Bufford, Z. Bi, Q.X. Jia, H. Wang, X. Zhang, Nanotwins and stacking faults in high-strength epitaxial Ag/Al multilayer films, Appl. Phys. Lett. 101 (2012), 223112
- [31] J. McKeown, A. Misra, H. Kung, R.G. Hoagland, M. Nastasi, Microstructures and strength of nanoscale Cu–Ag multilayers, Scr. Mater. 46 (2002) 593–598.
- [32] A.F. Jankowski, J.P. Hayes, C.K. Saw, Dimensional attributes in enhanced hardness of nanocrystalline Ta-V nanolaminates, Philos. Mag. 87 (2007) 2323–2334.

- [33] Y.F. Zhang, S. Xue, Q. Li, J. Li, J. Ding, T.J. Niu, R. Su, H. Wang, X. Zhang, Size dependent strengthening in high strength nanotwinned Al/Ti multilayers, Acta Mater 175 (2019) 466–476.
- [34] R. Su, D. Neffati, Q. Li, S. Xue, J. Cho, J. Li, J. Ding, Y. Zhang, C. Fan, H. Wang, Ultra-high strength and plasticity mediated by partial dislocations and defect networks: Part I: texture effect, Acta Mater 185 (2020) 181–192.
- [35] M. Nasim, Y. Li, M. Dargusch, C. Wen, Ultra-strong and ductile Ta/Co nanolaminates strengthened via grain-boundary expanding and interfacial sliding, Appl. Mater. Today 23 (2021), 100983.
- [36] X.F. Zhu, Y.P. Li, G.P. Zhang, J. Tan, Y. Liu, Understanding nanoscale damage at a crack tip of multilayered metallic composites, Appl. Phys. Lett. 92 (2008), 161905.
- [37] J.Y. Zhang, F.L. Zeng, K. Wu, Y.Q. Wang, X.Q. Liang, G. Liu, G.J. Zhang, J. Sun, Size-dependent plastic deformation characteristics in He-irradiated nanostructured Cu/Mo multilayers: competition between dislocation-boundary and dislocationbubble interactions, Mater. Sci. & Eng. A 673 (2016) 530–540.
- [38] A. Misra, J.P. Hirth, R.G. Hoagland, Length-scale-dependent deformation mechanisms in incoherent metallic multilayered composites, Acta Mater 53 (2005) 4817–4824.
- [39] E.G. Fu, N. Li, A. Misra, R.G. Hoagland, H. Wang, X. Zhang, Mechanical properties of sputtered Cu/V and Al/Nb multilayer films, Mater. Sci. & Eng. A 493 (2008) 283–287.
- [40] J.M. Wheeler, R. Raghavan, V. Chawla, J. Zechner, I. Utke, J. Michler, Failure mechanisms in metal–metal nanolaminates at elevated temperatures: microcompression of Cu–W multilayers, Scr. Mater. 98 (2015) 28–31.
- [41] Y. Cui, B. Derby, N. Li, N.A. Mara, A. Misra, Suppression of shear banding in highstrength Cu/Mo nanocomposites with hierarchical bicontinuous intertwined structures, Mater. Res. Lett. 6 (2018) 184–190.
- [42] T. Zhu, J. Li, A. Samanta, A. Leach, K. Gall, Temperature and strain-rate dependence of surface dislocation nucleation, Phys. Rev. Lett. 100 (2008), 025502.
- [43] C.R. Weinberger, A.T. Jennings, K. Kang, J.R. Greer, Atomistic simulations and continuum modeling of dislocation nucleation and strength in gold nanowires, J. Mech. Phys. Solids 60 (2012) 84–103.
- [44] Y. Fan, Y.N. Osetsky, S. Yip, B. Yildiz, Onset mechanism of strain-rate-induced flow stress upturn, Phys. Rev. Lett. 109 (2012), 135503.
- [45] Z.T. Bai, Y. Fan, Abnormal strain rate sensitivity driven by a unit dislocationobstacle interaction in bcc Fe, Phys. Rev. Lett. 120 (2018), 125504.
- [46] X.Z. Tang, Y.F. Guo, L.X. Sun, Y. Fan, S. Yip, B. Yildiz, Strain rate effect on dislocation climb mechanism via self-interstitials, Mater. Sci. & Eng. A 713 (2018) 141–145.
- [47] I. Szlufarska, Atomistic simulations of nanoindentation, Mater, Today 9 (2006) 42–50.
- [48] V. Yamakov, D. Wolf, S.R. Phillpot, A.K. Mukherjee, H. Gleiter, Dislocation processes in the deformation of nanocrystalline aluminium by molecular-dynamics simulation 1 (2002) 45–49.
- [49] A. Stukowski, Structure identification methods for atomistic simulations of crystalline materials, Model. Simul. Mater. Sci. Eng. 20 (4) (2012), 045021.
- [50] D. Rodney, C. Schuh, Distribution of thermally activated plastic events in a flowing glass, Phys. Rev. Lett. 102 (2009), 235503.
- [51] Y. Wang, Y. Fan, Incident velocity induced nonmonotonic aging of vapor-deposited polymer glasses, J. Phys. Chem. B 124 (2020) 5740–5745.
- [52] W.M. Choi, Y.H. Jo, S.S. Sohn, S. Lee, B.J. Lee, Understanding the physical metallurgy of the CoCrFeMnNi high-entropy alloy: an atomistic simulation study, npj Comput. Mater. 4 (1) (2018) 1.
- [53] H.S. Oh, S.J. Kim, K. Odbadrakh, W.H. Ryu, K.N. Yoon, S. Mu, F. Körmann, Y. Ikeda, C.C. Tasan, D. Raabe, T. Egami, E.S. Park, Engineering atomic-level complexity in high-entropy and complex concentrated alloys, Nat. Commun. 10 (1) (2019) 2090.
- [54] J.B. Mann, T.L. Meek, E.T. Knight, J.F. Capitani, L.C. Allen, Configuration energies of the d-block elements, J. Am. Chem. Soc. 122 (21) (2000) 5132–5137.
- [55] D.W. Smith, Electronegativity in two dimensions: reassessment and resolution of the Pearson-Pauling paradox, J. Chem. Educ. 67 (11) (1990) 911.
- [56] L. Jiang, Y.J. Hu, K. Sun, P.Y. Xiu, M. Song, Y.W. Zhang, W.L. Boldman, M. L. Crespillo, P.D. Rack, L. Qi, W.J. Weber, L.M. Wang, Irradiation-induced extremes create hierarchical face-/body-centered-cubic phases in nanostructured high entropy alloys, Advanced Mater 39 (32) (2020), 2002652.
- [57] N. Chen, R. Frank, N. Asao, D.V. Louzguine-Luzgin, P. Sharma, J.Q. Wang, G. Q. Xie, Y. Ishikawa, N. Hatakeyama, Y.C. Lin, Formation and properties of Aubased nanograined metallic glasses, Acta Mater 59 (2011) 6433–6440.
- [58] F.C. Li, T.Y. Wang, Q.F. He, B.A. Sun, C.Y. Guo, T. Feng, Y. Yang, Micromechanical mechanism of yielding in dual nano-phase metallic glass, Scr. Mater. 154 (2018) 186–191.
- [59] J.X. Fang, U. Vainio, W. Puff, R. Würschum, X.L. Wang, D. Wang, M. Ghafari, F. Jiang, J. Sun, H. Hahn, Atomic structure and structural stability of Sc75Fe25 nanoglasses, Nano. Lett. 12 (2011) 458–463.
- [60] J.Q. Wang, N. Chen, P. Liu, Z. Wang, D.V. Louzguine-Luzgin, M.W. Chen, J. H. Perepezko, The ultrastable kinetic behavior of an Au-based nanoglass, Acta Mater 79 (2014) 30–36.
- [61] H. Gleiter, Our thoughts are ours, their ends none of our own: are there ways to synthesize materials beyond the limitations of today? Acta Mater 56 (2008) 5875–5893.
- [62] H. Gleiter, T. Schimmel, H. Hahn, Nanostructured solids-From nano-glasses to quantum transistors, Nano. Today 9 (2014) 17–68.
- [63] R. Witte, T. Feng, J.X. Fang, A. Fischer, M. Ghafari, R. Kruk, R.A. Brand, D. Wang, H. Hahn, H. Gleiter, Evidence for enhanced ferromagnetism in an iron-based nanoglass, Appl. Phys. Lett. 103 (2013) 73106.

- [64] C. Guo, Y. Fang, B. Wu, S. Lan, G. Peng, X. Wang, H. Hahn, H. Gleiter, T. Feng, Ni-P nanoglass prepared by multi-phase pulsed electrodeposition, Mater. Res. Lett. 5 (2016) 293–299.
- [65] D. Danilov, H. Hahn, H. Gleiter, W. Wenzel, Mechanisms of nanoglass ultrastability, ACS Nano 10 (2016) 3241–3247.
- [66] X. Wang, F. Jiang, H. Hahn, J. Li, H. Gleiter, J. Sun, J. Fang, Sample size effects on strength and deformation mechanism of Sc75Fe25 nanoglass and metallic glass, Scr. Mater. 116 (2016) 95–99.
- [67] X.L. Wang, F. Jiang, H. Hahn, J. Li, H. Gleiter, J. Sun, J.X. Fang, Plasticity of a scandium-based nanoglass, Scr. Mater. 98 (2015) 40–43.
- [68] N. Chen, D.V. Louzguine-Luzgin, G.Q. Xie, P. Sharma, J.H. Perepezko, M. Esashi, A. R. Yavari, A. Inoue, Structural investigation and mechanical properties of a representative of a new class of materials: nanograined metallic glasses, Nanotechnology 24 (2013) 45610.
- [69] O.N. Senkov, J.M. Scott, S.V. Senkova, F. Meisenkothen, D.B. Miracle, C. F. Woodward, Microstructure and elevated temperature properties of a refractory TaNbHfZrTi alloy, J. Mater. Sci. 47 (2012) 4062–4074.
- [70] P. Hruška, F. Lukáč, S. Cichoň, M. Vondráček, J. Čížek, L. Fekete, J. Lančok, J. Veselý, P. Minárik, M. Cieslar, O. Melikhova, T. Kmječ, M.O. Liedke, M. Butterling, A. Wagner, Oxidation of amorphous HfNbTaTiZr high entropy alloy thin films prepared by DC magnetron sputtering, J. Alloy Compd. 869 (2021), 157978
- [71] S. Fritze, C.M. Koller, L. Fieandt, P. Malinovskis, K. Johansson, E. Lewin, P. H. Mayrhofer, U. Jansson, Influence of deposition temperature on the phase evolution of HfNbTiVZr high-entropy thin films, Materials 12 (2019) 587.
- [72] T.W. Barbee, B.E. Jacobson, D.L. Keith, Microstructure of amorphous 304-stainless steel-carbon alloys synthesized by magnetron sputter deposition, Thin Solid Films 63 (1979) 143.
- [73] Z. Wang, C. Wang, Y. Zhao, T. Huang, C. Li, J. Kai, C. Liu, C. Hsueh, Growth, microstructure and mechanical properties of CoCrFeMnNi high entropy alloy films, Vacuum 179 (2020), 109553.
- [74] G. Dirras, L. Lilensten, P. Djemia, M. Laurent-Brocq, D. Tingaud, J.P. Couzinié, L. Perrière, T. Chauveau, I. Guillot, Elastic and plastic properties of as-cast equimolar TiHfZrTaNb high-entropy alloy, Mater. Sci. & Eng. A 654 (2016) 30–38.
- [75] N. Tüten, D. Canadinc, A. Motallebzadeh, B. Bal, Microstructure and tribological properties of TiTaHfNbZr high entropy alloy coatings deposited on Ti6Al4V substrates, Intermetallics 105 (2019) 99–106.
- [76] M. Wei, Z. Cao, X. Meng, Interfacial structures governed plastic deformation behaviors in metallic multilayers, Acta Metall. Sin-Engl 29 (2016) 199–204.
- [77] L. Jiang, M. Powers, Y. Cui, B.K. Derby, A. Misra, Microstructure and mechanical properties of nanoscale Cu/(Ta50Nb25Mo25) multilayers, Mater. Sci. & Eng. A 799 (2021), 0921-5093.
- [78] J.H. Perepezko, S.D. Imhoff, M.W. Chen, J.Q. Wang, S. Gonzalez, Nucleation of shear bands in amorphous alloys, Proc. Natl. Acad. Sci. 111 (2014) 3938–3942.
- [79] Y. Zhang, A.L. Greer, Thickness of shear bands in metallic glasses, Appl. Phys. Lett. 89 (2006) 71907.

- [80] Y.P. Li, X.F. Zhu, G.P. Zhang, J. Tan, W. Wang, B. Wu, Investigation of deformation instability of Au/Cu multilayers by indentation, Philos. Mag. 90 (2010) 3049–3067.
- [81] D. Wang, T. Kups, J. Schawohl, P. Schaaf, Deformation behavior of Au/Ti multilayers under indentation, J. Mater. Sci. Mater. Electron. 23 (2012) 1077–1082.
- [82] G.P. Zhang, Y. Liu, W. Wang, J. Tan, Experimental evidence of plastic deformation instability in nanoscale Au/Cu multilayers, Appl. Phys. Lett. 88 (2006), 13105.
- [83] S.V. Madge, D.V. Louzguine-Luzgin, J.J. Lewandowski, A.L. Greer, Toughness, extrinsic effects and Poisson's ratio of bulk metallic glasses, Acta Mater 60 (2012) 4800–4809.
- [84] R. Maaß, D. Klaumünzer, E.I. Preiß, P.M. Derlet, J.F. Löffler, Single shear-band plasticity in a bulk metallic glass at cryogenic temperatures, Scr. Mater. 66 (2012) 231–234.
- [85] J. Pan, L. Liu, K.C. Chan, Enhanced plasticity by phase separation in CuZrAl bulk metallic glass with micro-addition of Fe, Scr. Mater. 60 (2009) 822–825.
- [86] S. Adibi, P.S. Branicio, Y. Zhang, S.P. Joshi, Composition and grain size effects on the structural and mechanical properties of CuZr nanoglasses, J. Appl. Phys. 116 (2014) 43522.
- [87] S. Adibi, P.S. Branicio, S.P. Joshi, Suppression of shear banding and transition to necking and homogeneous flow in nanoglass nanopillars, Sci. Rep. 5 (2015) 15611.
- [88] T. Wang, L. Wang, Q. Wang, Y. Liu, X. Hui, Pronounced plasticity caused by phase separation and β-relaxation synergistically in Zr–Cu–Al–Mo bulk metallic glasses, Sci. Rep. 7 (2017) 1238.
- [89] S. Adibi, Z. Sha, P.S. Branicio, S.P. Joshi, Z. Liu, Y. Zhang, A transition from localized shear banding to homogeneous superplastic flow in nanoglass, Appl. Phys. Lett. 103 (2013), 211905.
- [90] G. Wu, S. Balachandran, B. Gault, W. Xia, C. Liu, Z. Rao, Y. Wei, S. Liu, J. Lu, M. Herbig, Crystal–glass high-entropy nanocomposites with near theoretical compressive strength and large deformability, Adv. Mater. 32 (2020), 2002619.
- [91] Y. Wu, Y. Xiao, G. Chen, C.T. Liu, Z. Lu, Bulk metallic glass composites with transformation-mediated work-hardening and ductility, Adv. Mater. 22 (2010) 2770–2773.
- [92] W. Guo, E. Jägle, J. Yao, V. Maier, S. Korte-Kerzel, J.M. Schneider, D. Raabe, Intrinsic and extrinsic size effects in the deformation of amorphous CuZr/ nanocrystalline Cu nanolaminates, Acta Mater 80 (2014) 94–106.
- [93] Y.Q. Wang, K. Wu, J.Y. Zhang, G. Liu, J. Sun, Probing the size- and constituent-mediated mechanical properties and deformation behavior in crystalline/amorphous nanolaminates, Nanoscale 10 (2018) 21827–21841.
- [94] J.Y. Zhang, G. Liu, S.Y. Lei, J.J. Niu, J. Sun, Transition from homogeneous-like to shear-band deformation in nanolayered crystalline Cu/amorphous Cu–Zr micropillars: intrinsic vs. extrinsic size effect, Acta Mater 60 (2012) 7183–7196.
- [95] X. Zhang, A. Misra, H. Wang, M. Nastasi, J.D. Embury, T.E. Mitchell, R. G. Hoagland, J.P. Hirth, Nano-scale twinning induced strengthening in austenitic stainless steel thin films. Appl. Phys. Lett. 84 (2004) 1096.
- [96] X. Zhang, H. Wang, X.H. Chen, L. Lu, K. Lu, R.G. Hoagland, A. Misra, High-strength sputter-deposited Cu foils with preferred orientation of nanoscale growth twins, Appl. Phys. Lett. 88 (2006), 173116.